Double-strangeness production in $\Lambda p \to K^+ X$ reaction

Jung Keun Ahn[1] and Seung-il Nam[2,3,*]

[1]*Department of Physics, Korea University, Seoul 02841, Republic of Korea*
[2]*Department of Physics and Institute for Radiation Science & Technology (IRST), Pukyong National University, Busan 48513, Republic of Korea*
[3]*Asia Pacific Center for Theoretical Physics (APCTP), Pohang 37673, Republic of Korea*

(Received 31 January 2021; accepted 28 May 2021; published 22 June 2021)

We investigate $S = -2$ production from the $\Lambda p \to K^+ X$ reactions within the effective Lagrangian approach. The $\Lambda p \to K^+ \Lambda\Lambda$ and $\Lambda p \to K^+ \Xi^- p$ reactions are considered to find the lightest $S = -2$ system, which is H-dibaryon. We assume that the $H(2250) \to \Lambda\Lambda$, and $H(2270) \to \Xi^- p$ decays with the intrinsic decay width of 1 MeV. According to our calculations, the total cross sections for $\Lambda p \to K^+ \Lambda\Lambda$ and $\Lambda p \to K^+ \Xi^- p$ reactions were found to be of the order of a few μb in the Λ beam momentum range of up to 5 GeV/c. Furthermore, the direct access of information regarding the interference patterns between the H-dibaryon and nonresonant contributions was demonstrated.

DOI: 10.1103/PhysRevD.103.114022

I. INTRODUCTION

Double-strangeness baryon systems involve an H-dibaryon, double hypernuclei, and possibly the inner core of neutron stars [1]. An observation of several double hypernuclei reveals that the $\Lambda\Lambda$ interaction is weakly attractive. However, the $\Xi^- N$ interaction was only studied in heavy-ion collisions, which indicates a strong, attractive interaction [2]. Recently, the ΞN–$\Lambda\Lambda$ coupling was determined to be weak based on an initial observation of a Coulomb-assisted bound state for the Ξ^-–^{14}N system [3], which was predicted to exist considering the evidence for a deeply bound Ξ^-–^{14}N state reported in a hybrid emulsion experiment at KEK-PS [4]. While strangeness $S = -2$ baryon-baryon interactions provide critical information on exploring the smallest object (H-dibaryon), and the largest (the inner core of neutron stars), the experimental data is limited.

The lightest $S = -2$ system is the H-dibaryon, which can be decomposed into a compact 6-quark state, and two baryon states involving $\Lambda\Lambda$, ΞN, and $\Sigma\Sigma$ components. The mass range of the H-dibaryon is strongly connected with the existence of double Λ hypernuclei. Several double Λ hypernuclei have been reported: ${}^{6}_{\Lambda\Lambda}$He [5], ${}^{10}_{\Lambda\Lambda}$Be [6], and ${}^{13}_{\Lambda\Lambda}$B [7]. Because the $\Lambda\Lambda \to H$ decay was not observed in the aforementioned studies, the H must be heavier than $m_H > 2m_\Lambda + B_{\Lambda\Lambda} \approx 2.22$ GeV/c^2.

In Refs. [8–10], the strangeness $S = -2$ baryon-baryon interactions in chiral effective field theories were investigated with lattice-QCD data. Li and his colleagues [8] scrutinizes the analyses of the lattice-QCD data with caution in terms of the use of isospin symmetry, chiral extrapolations, and the dependence on the lattice time. From the $2N_f$ 'tHooft interaction induced by the instanton, the six-quark interaction is investigated for the dibaryon using the quark-cluster model and turns out to be repulsive eliminating the dibaryon [11]. From the relativistic collision experiments such as the STAR and ALICE collaborations, the dibaryon formation has been explored to estimate the $\Lambda\Lambda$ interactions in terms of their binding energy [12,13]. For instance, the binding energy is estimated within an effective-range expansion approach with $B_{\Lambda\Lambda} = 3.2^{+1.6}_{-2.4}(\text{stat})^{+1.8}_{-1.0}(\text{syst})$ MeV from the $\Lambda\Lambda$ femtoscopic measurements [13]. The holographic QCD approach is also applied to investigate the dibaryon, which is n described as an SO(3)-type topological soliton with $B = 2$, resulting in $M_H \approx 1.7$ GeV [14,15]. In Ref. [16], the authors studied the dibaryon with that the two strange quarks are in the spin-0 state by using the quark model, resulting in no compact bound states found. It is also important to note that lattice QCD simulations have been the most active field for the dibaryon searches for decades [17–21], although its existence has not been fully supported. Among them, recently, the HAL QCD collaboration has indicated that the $\Lambda\Lambda(^1S_0)$ interaction is not sufficiently attractive to generate a bound or resonant state close to the $\Lambda\Lambda$ threshold, whereas the $\Xi N(^1S_0)$ phase shift increases sharply just above the ΞN threshold [22]. Experimental

*sinam@pknu.ac.kr

confirmation of the H-dibaryon would be a significant accomplishment for a better understanding of hyperon interactions.

Enhanced $\Lambda\Lambda$ production close to the $\Lambda\Lambda$ threshold was reported in $^{12}\mathrm{C}(K^-, K^+)$ reactions at $p_{K^-} = 1.65$ GeV/c [23,24]. This threshold enhancement may provide insight for the possible existence of an H-dibaryon near the $\Lambda\Lambda$ or $\Xi^- p$ thresholds. A high-statistics experimental reconfirmation should be awaited until the dedicated H-dibaryon search experiment E42 [25] is performed using a high-intensity K^- beam at J-PARC.

The simplest method for producing the H-dibaryon is to employ the double-strangeness and double-charge exchange (K^-, K^+) reaction on a light nuclear target to retain two units of strangeness in a ^{12}C nucleus, similar to the J-PARC E42 with a diamond target at $p_{K^-} = 1.8$ GeV/c. Furthermore, the H-dibaryon is also available in other reactions, such as pp, pA, γA, and πA, most of which involve nuclear targets that contain at least two nucleons coupled to the H-dibaryon production; therefore, the overlap of wave functions for hyperons and intranuclear nucleons should be considered. A cross section measurement for the $\Lambda\Lambda$ production was reported to be 6.7 ± 1.5 mb in a $\bar{p}$-Ta reaction at 4 GeV/c [26]. Heavy-ion reactions can be used to produce Λ and Ξ^- hyperons copiously so that the coalescence of two of these particles into the H-dibaryon may be observed. However, the H-dibaryon should be observed in a high-multiplicity environment for high-energy heavy-ion collisions.

Because the H-dibaryon can be formed directly via ΞN and $\Lambda\Lambda$ interactions, the production reaction involving the minimum number of vertices is the $\Xi^- p \to H$ reaction with a proton target. However, in this case, the mass range of the H-dibaryon is accessible only above the $\Xi^- p$ mass threshold. Because a $\Lambda\Lambda$ scattering experiment is unavailable, the second-best choice is a $\Lambda p \to HK^+$ reaction via a strangeness-exchange process, with which the H-dibaryon can be observed in the mass range below the $\Lambda\Lambda$ threshold to a higher mass region.

A Λ beam is available via photoproduction and π^--induced reactions by tagging K^+, K^0, or $K(892)^*$ in the final state. For example, the π^--induced reactions can either be a $\pi^- p \to K^0\Lambda$ or $\pi^- p \to K(892)^*\Lambda$ reaction. As the detection of a $K^0_S \to 2\pi$ decay triggers the production of both $S = +1$ K^0 and $S = -1$ $\bar{K}^0$ with nearly equal probability, the production of Λ particles cannot be uniquely tagged. Therefore, the $\pi^- p \to K(892)^*\Lambda$ reaction is selected as a primary reaction for the Λp elastic scattering measurement using an 8 GeV/c π^- beam at J-PARC [27]. In this case, the Λ beam is available in the momentum ranging from 0.2 to 2.0 GeV/c, and it is unavailable for double-strangeness production above the threshold Λ momentum of 2.6 GeV/c.

However, the $\gamma p \to K^+\Lambda$ reaction facilitates the production of a high-momentum Λ with Λ polarization in the photon beam energy region above 2.5 GeV. The measurement of $\Lambda p \to K^+\Lambda\Lambda$ and $\Lambda p \to K^+\Xi^- p$ is viable with the CLAS data [28] and the upcoming LEPS2 data [29]. This (Λ, K^+) reaction measurement leads to a decisive conclusion regarding the existence of the H-dibaryon near the $\Lambda\Lambda$ and $\Xi^- p$ thresholds. Moreover, possible interference effects among the $K^+\Lambda\Lambda$ and $K^+\Xi^- p$ channels are noteworthy.

In this study, numerical calculation results for the $\Lambda p \to K^+\Lambda\Lambda$ and $\Lambda p \to K^+\Xi^- p$ reactions within the effective Lagrangian approach have been reported. We calculate the Dalitz plot densities $(d^2\sigma/dM_{\Lambda\Lambda}dM_{\Lambda K^+})$ for the $\Lambda p \to K^+\Lambda\Lambda$ reaction and $(d^2\sigma/dM_{\Xi^- p}dM_{\Xi^- K^+})$ for the $\Lambda p \to K^+\Xi^- p$ reaction. The H-dibaryon states are assumed to appear at 2.25 GeV/c^2 and 2.27 GeV/c^2 in the $\Lambda\Lambda$ and $\Xi^- p$ channels, respectively. The intrinsic width of the H-dibaryon was chosen to be 1 MeV. Based on calculations, the total cross sections for the $\Lambda p \to K^+\Lambda\Lambda$ and $\Lambda p \to K^+\Xi^- p$ reactions were determined to be within the order of a few μb in the Λ beam momentum of up to 5 GeV/c. Furthermore, we demonstrated that information regarding the interference patterns between the H-dibaryon and non-resonant contributions can be directly accessed.

II. THEORETICAL FRAMEWORK

In this section, we introduce the theoretical framework to investigate the $\Lambda p \to K^+X$ reactions within the effective Lagrangian approach. We consider the $\Lambda p \to K^+\Lambda\Lambda$ and $\Lambda p \to K^+\Xi^- p$ reactions. The relevant Feynman diagrams for the reactions are illustrated in Figs. 1 and 2. Diagrams (a) and (b) indicate an H-dibaryon-pole with Λ and Ξ exchanges, respectively. The other diagrams $(c$–$f)$ denote various baryon-pole contributions with t-channel meson

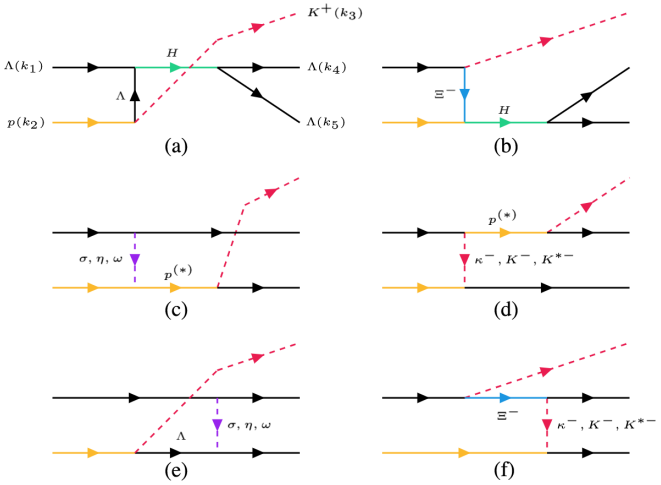

FIG. 1. Relevant Feynman diagrams for the present reaction processes of $\Lambda p \to K^+\Lambda\Lambda$ at the tree level. Diagrams (a) and (b) indicate the H-dibaryon-pole contributions with the Λ and Ξ exchanges. Diagrams $(c$–$f)$ denote the various baryon-pole contributions with the strange and nonstrange meson exchanges in the t-channel.

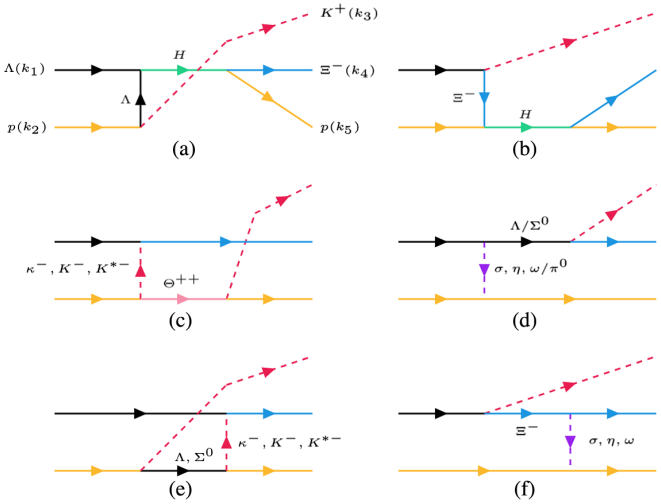

FIG. 2. Corresponding Feynman diagrams for the reaction processes of $\Lambda p \to K^+\Xi^- p$ at the tree level. Diagrams (a) and (b) indicate the H-dibaryon-pole contributions with the Λ and Ξ exchanges. Diagrams (c–f) denote the various baryon-pole contributions with the strange and non-strange meson exchanges in the t-channel.

exchanges. The effective Lagrangians for the Yukawa vertices are defined as follows:

$$\begin{aligned}
\mathcal{L}_{BBH} &= -g_{BBH} B^\dagger B^\dagger H + \text{H.c.},\\
\mathcal{L}_{BBH} &= g_{BBBB} B^\dagger B^\dagger \Gamma B B + \text{H.c.},\\
\mathcal{L}_{SBB} &= -i g_{SBB} \bar{B} S B + \text{H.c.},\\
\mathcal{L}_{PBB} &= -i g_{MBB} \bar{B} \gamma_5 P B + \text{H.c.},\\
\mathcal{L}_{PBB'} &= -i g_{MBB'} \bar{B}' P B + \text{H.c.},\\
\mathcal{L}_{VBB} &= g_{VBB} \bar{B} \not{V} B + \text{H.c.},
\end{aligned} \tag{1}$$

where B, B', H, S, P, and V denote the fields for the $1/2^+$ baryon, $1/2^-$ baryon, $S = -2$ isoscalar-scalar H dibaryon [30], scalar meson, pseudoscalar meson, and vector meson, respectively. The coupling constant $g_{BB'H}$ is given by $g_{\Lambda\Lambda H} = -g/\sqrt{8}$ and $g_{N\Xi H} = -g/\sqrt{2}$, where $g \approx 2.4/\sqrt{\text{MeV}}$ is used to reproduce the HAL-QCD collaboration results in the flavor SU(3) limit [30,31]. The values of $g_{(S,P,V)BB}$ are obtained from the Nijmegen soft-core model (NSC) [32], whereas those for $g_{PBB'}$ are determined by the experimental results [33] and the SU(3) relations. All the relevant couplings for $\Lambda p \to K^+\Lambda\Lambda$ and $\Lambda p \to K^+\Xi^- p$ are listed in Table I.

Diagrams (a) and (b) for the $\Lambda p \to K^+\Lambda\Lambda$ ($\Lambda\Lambda$ channel in the following) can be computed using these Lagrangians, resulting in the following invariant amplitudes:

$$\begin{aligned}
i\mathcal{M}^{\Lambda\Lambda}_{(a)} &= g_{KN\Lambda} g^2_{\Lambda\Lambda H} u_5^\dagger [u_4^\dagger D^0_H(q_{4+5}) u_1] D^{1/2}_\Lambda(q_{2-3}) \gamma_5 u_2\\
&\quad - (4 \leftrightarrow 5),
\end{aligned} \tag{2}$$

TABLE I. Values of the full decay widths for the relevant hadrons from Refs. [33].

h	σ	η	ω	κ	K
Γ_h [MeV]	550	1.31	8.49	478	0

h	K^*	(N, Λ, Ξ)	$N^*(1650)$
Γ_h [MeV]	50.8	0	158.2

$$\begin{aligned}
i\mathcal{M}^{\Lambda\Lambda}_{(b)} &= \frac{1}{\sqrt{2}} g_{K\Lambda\Xi} g_{N\Xi H} g_{\Lambda\Lambda H} u_4^\dagger u_5^\dagger D^0_H(q_{4+5}) u_2\\
&\quad \times D^{1/2}_\Xi(q_{1-3}) \gamma_5 u_1 - (4 \leftrightarrow 5),
\end{aligned} \tag{3}$$

where $q_{i\pm j} \equiv k_i \pm k_j$ and D^s_h indicate the *dressed* propagator for a hadron h with spin s. Its explicit form in the present work is as follows:

$$D^0_h(q) = \frac{F_h(q^2)}{q^2 - M_h^2 - i\Gamma_h M_h}, \tag{4}$$

$$D^1_{h\mu\nu}(q) = \frac{F_h(q^2)}{q^2 - M_h^2 - i\Gamma_h M_h}\left(g_{\mu\nu} - \frac{q_\mu q_\nu}{M_h^2}\right), \tag{5}$$

$$D^{1/2}_h(q) = \frac{(\not{q} + M_h) F_h(q^2)}{q^2 - M_h^2 - i\Gamma_h M_h}. \tag{6}$$

Here, the factors M_h, Γ_h, and q, denote the mass and full decay width of the hadron h, and the transferred momentum, respectively. The values of Γ_h are listed in Table I. The phenomenological form factor F_h presents the spatial extension of the hadron h. In this study, we employ the following type of the form factors:

$$F_h(q^2) = \frac{\Lambda_h^4}{\Lambda_h^4 + (M_h^2 - q^2)^2}. \tag{7}$$

The cutoff mass Λ_h is determined from other experimental data in the next section. Notably, the interchange of the Λ baryons in the final state ($4 \leftrightarrow 5$) in Eq. (2) gives a negative sign, owing to the Fermi-Dirac statistics. All the relevant meson-baryon couplings are obtained from the Nijmegen soft-core potential model [32], as listed in Table II.

The invariant amplitudes for the diagram (c) can be evaluated as follows:

TABLE II. Relevant coupling constants for the present reaction process. These values are obtained from Refs. [30–32,34,35]. Here, σ and N^* denote $f_0(500, 0^+)$ and $N^*(1650, 1/2^-)$, which is the most important contribution in the vicinity of the production threshold.

$\Lambda\Lambda H$	$N\Xi H$	$(\kappa, K, K^*)N\Lambda$	$(\kappa, K, K^*)\Lambda\Xi$	$(\sigma, \eta, \omega)NN$	$(\sigma, \eta, \omega)\Lambda\Lambda$	$(\sigma, \eta, \omega)\Xi\Xi$
$\frac{-1.2}{\sqrt{2}\ \mathrm{MeV}}$	$\frac{-2.4}{\sqrt{2}\ \mathrm{MeV}}$	$(-8.31, -13.4, -4.26)$	(8.77,3.92,4.26)	$(-0.50, 6.34, 10.4)$	$(-6.45, -6.86, 4.96)$	$(-12.6, -11.1, 1.95)$

$KN^*\Lambda$	ηNN^*	$(\kappa, K, K^*)N\Sigma$	$(\kappa, K, K^*)\Lambda\Xi$	$(\kappa, K, K^*)\Sigma\Xi$	$\pi\Lambda\Sigma$	πNN
0.53	0.35	$(-5.32, -4.09, -2.46)$	(8.77,3.92,4.26)	$(-4.54, -16.7, -2.46)$	11.9	13.0

$$i\mathcal{M}^{\sigma p}_{(c)} = -g_{\sigma\Lambda\Lambda}g_{KN\Lambda}g_{\sigma NN}[\bar{u}_5\gamma_5 D_p^{1/2}(q_{3+5})u_2]D^0_\sigma(q_{1-4})[\bar{u}_4 u_1] - (4 \leftrightarrow 5), \tag{8}$$

$$i\mathcal{M}^{\eta p}_{(c)} = -g_{\eta\Lambda\Lambda}g_{KN\Lambda}g_{\eta NN}[\bar{u}_5\gamma_5 D_p^{1/2}(q_{3+5})\gamma_5 u_2]D^0_\eta(q_{1-4})[\bar{u}_4\gamma_5 u_1] - (4 \leftrightarrow 5), \tag{9}$$

$$i\mathcal{M}^{\omega p}_{(c)} = -g_{\omega\Lambda\Lambda}g_{KN\Lambda}g_{\omega NN}[\bar{u}_5\gamma_5 D_p^{1/2}(q_{3+5})\gamma^\mu(q_{1-4})u_2]D^1_{\omega\mu\nu}[\bar{u}_4\gamma^\nu u_1] - (4 \leftrightarrow 5). \tag{10}$$

$$i\mathcal{M}^{\eta p^*}_{(c)} = -g_{\eta\Lambda\Lambda}g_{KN^*\Lambda}g_{\eta NN^*}[\bar{u}_5 D_{p^*}^{1/2}(q_{3+5})u_2]D^0_\eta(q_{1-4})[\bar{u}_4\gamma_5 u_1] - (4 \leftrightarrow 5), \tag{11}$$

for the (σ, η, ω) meson exchange in the t-channel. The superscripts in $i\mathcal{M}^{h_1h_2}_{(c)}$ denote the intermediate hadrons as shown in Fig. 1. Regarding the nucleon-resonance and Δ-baryon contributions, we only consider the couplings to the η meson to avoid theoretical uncertainties.

The scalar meson σ represents $f_0(500, 0^+)$ [33]. For the production of H-dibaryon near the threshold ($\sqrt{s} \approx 2725$ MeV), only the nucleon resonance $N^*(1650, 1/2^-)$ becomes relevant to the amplitude, $i\mathcal{M}^{\eta p^*}_{(c)}$. The strong coupling constants corresponding to $N^*(1650, 1/2^-)$ are also obtained from the chiral coupled-channel method [34], as listed in Table II. Similarly, the (κ, K, K^*) meson-exchange contributions are as follows:

$$\mathcal{M}^{\kappa^- p}_{(d)} = -g_{KN\Lambda}g^2_{\kappa N\Lambda}[\bar{u}_4\gamma_5 D_p^{1/2}(q_{3+4})u_1]D^0_\kappa(q_{5-2})[\bar{u}_5 u_2] - (4 \leftrightarrow 5), \tag{12}$$

$$i\mathcal{M}^{K^- p}_{(d)} = -g_{KN\Lambda}g^2_{KN\Lambda}[\bar{u}_4\gamma_5 D'^{1/2}_p(q_{3+4})\gamma_5 u_1]D^0_{K^-}(q_{5-2})[\bar{u}_5\gamma_5 u_2] - (4 \leftrightarrow 5), \tag{13}$$

$$\mathcal{M}^{K^{*-} p}_{(d)} = -g_{KN\Lambda}g^2_{K^*N\Lambda}[\bar{u}_4\gamma_5 D_p^{1/2}(q_{3+4})\gamma^\mu u_1]D^1_{K^*\mu\nu}(q_{5-2})[\bar{u}_5\gamma^\nu u_2] - (4 \leftrightarrow 5) \tag{14}$$

$$i\mathcal{M}^{K^- p^*}_{(d)} = -g_{KN\Lambda}g^2_{KN^*\Lambda}[\bar{u}_4 D_{p^*}^{1/2}(q_{3+4})u_1]D^0_{K^-}(q_{5-2})[\bar{u}_5\gamma_5 u_2] - (4 \leftrightarrow 5), \tag{15}$$

where the strange scalar meson denotes $\kappa^-(800)$ [33].

The background contributions, which do not form resonant band structures in the Dalitz plot, are given by the following:

$$i\mathcal{M}^{\sigma\Lambda}_{(e)} = -g_{KN\Lambda}g^2_{\sigma\Lambda\Lambda}[\bar{u}_5 D_\Lambda^{1/2}(q_{2-3})\gamma_5 u_2]D^0_\sigma(q_{1-4})[\bar{u}_4 u_1] - (4 \leftrightarrow 5), \tag{16}$$

$$i\mathcal{M}^{\eta\Lambda}_{(e)} = -g_{KN\Lambda}g^2_{\eta\Lambda\Lambda}[\bar{u}_5\gamma_5 D_\Lambda^{1/2}(q_{2-3})\gamma_5 u_2]D^0_\eta(q_{1-4})[\bar{u}_4\gamma_5 u_1] - (4 \leftrightarrow 5), \tag{17}$$

$$i\mathcal{M}^{\omega\Lambda}_{(e)} = -g_{KN\Lambda}g^2_{\omega\Lambda\Lambda}[\bar{u}_5\gamma_5\gamma^\mu D_\Lambda^{1/2}(q_{2-3})\gamma_5 u_2]D^1_{\omega,\mu\nu}(q_{1-4})[\bar{u}_4\gamma^\nu u_1] - (4 \leftrightarrow 5), \tag{18}$$

and

$$i\mathcal{M}^{\kappa^- p}_{(f)} = -g_{\kappa N\Lambda}g_{K\Lambda\Xi}g_{\kappa\Lambda\Xi}[\bar{u}_4 D_{\Xi^-}^{1/2}(q_{1-3})\gamma_5 u_1]D^0_{\kappa^-}(q_{5-2})[\bar{u}_5 u_2] - (4 \leftrightarrow 5), \tag{19}$$

$$i\mathcal{M}^{K^- p}_{(f)} = -g_{K\Lambda N}g_{K\Lambda\Xi}g_{K\Lambda\Xi}[\bar{u}_4\gamma_5 D_{\Xi^-}^{1/2}(q_{1-3})\gamma_5 u_1]D^0_{K^-}(q_{5-2})[\bar{u}_5\gamma_5 u_2] - (4 \leftrightarrow 5), \tag{20}$$

$$i\mathcal{M}^{K^{*-} p}_{(f)} = -g_{K^*N\Lambda}g_{K\Lambda\Xi}g_{K^*\Lambda\Xi}[\bar{u}_4\gamma^\mu D_{\Xi^-}^{1/2}(q_{1-3})\gamma_5 u_1]D^1_{K^*\mu\nu}(q_{5-2})[\bar{u}_5\gamma^\nu u_2] - (4 \leftrightarrow 5). \tag{21}$$

All the relevant coupling constants are provided in Table II.

For the $\Lambda p \to K^+ \Xi^- p$ reaction, we can compute the invariant amplitudes similarly without the particle-exchange $(4 \leftrightarrow 5)$ terms in the final state. The relevant coupling constants for this reaction are provided in Table II. In this reaction, the 27-plet Θ^{++} pentaquark contribution can be considered in diagram (c). However, the existence of this exotic baryon has never been confirmed experimentally. Hence, we ignore this contribution for brevity. In diagrams (d) and (e), there are two baryon-pole contributions, that is, Λ and Σ^0, which differ from the $\Lambda\Lambda$ channel.

Unlike the electromagnetic hadron production involving the Ward-Takahashi identity, determining the phase factors between strong-interaction amplitudes is a relatively difficult task owing to the lack of symmetry. In the present calculation, we employ a free parameter for the phase difference between the tree-level invariant amplitudes as follows:

$$i\mathcal{M}_{\rm tree} = i\mathcal{M}_{(a+b)} + e^{i\phi}[i\mathcal{M}_{(c+d+e+f)}]. \tag{22}$$

The phase factors among the invariant amplitudes of diagrams $(c$–$f)$, except for the nucleon-resonance contributions, are determined from the coupling constants in the Nijmegen model [32]. Although we do not have a theoretical reasoning for fixing the phase factor for the nucleon-resonance contributions, we simply assume that g_{MBN^*} is positively real. Moreover, the nucleon-resonance contributions were numerically verified to be negligible, owing to its significant full decay width as provided in Table I. Thus, we introduce a single phase factor between the H-dibaryon contributions and others, as shown in Eq. (22). The phase angle ϕ is considered a free parameter in the numerical calculations.

After attaining the aforementioned, the final-state interaction (FSI) contributions can be considered. The total amplitude including the FSI contributions is defined in the on-shell approximation (OnF) [36] as follows:

$$i\mathcal{M}^{\Lambda\Lambda,\rm OnF}_{\rm tree+FSI} = i\mathcal{M}^{\Lambda\Lambda}_{\rm tree} + \underbrace{(i\mathcal{M}^{\Lambda\Lambda}_{\rm tree})\left(i\int\frac{d^4q}{(2\pi)^4}\mathcal{G}^{\rm OnF}_{\Lambda\Lambda}\right)(i\hat{\mathcal{M}}^{\rm cc,OnF}_{\Lambda\Lambda\to\Lambda\Lambda})}_{\rm FSI}, \tag{23}$$

where $i\hat{\mathcal{M}}^{\rm cc,OnF}_{B_1B_2\to B_3B_4}$ stands for the flavor-singlet two-baryon coupling constant for the $I=0$ and $S=-2$ channels in the coupled-channel (cc) method. Based on the isospin symmetry, its elementary amplitude can be expressed as follows [37]:

$$i\hat{\mathcal{M}}_{B_1B_2\to B_3B_4} = -i\lambda_1\begin{pmatrix} +\frac{1}{8} & -\frac{1}{2} & -\frac{\sqrt{3}}{4} \\ -\frac{1}{2} & +\frac{1}{2} & +\frac{\sqrt{3}}{2} \\ -\frac{\sqrt{3}}{4} & +\frac{\sqrt{3}}{2} & +\frac{1}{8} \end{pmatrix}. \tag{24}$$

The value of λ_1 to reproduce the binding energy of the HAL QCD data is given by $-12.8/\mathrm{GeV}^2$ [37]. Note, in Eq. (23), only the baryon-baryon rescattering for FSI is considered for simplicity, and the $S=0$ meson-baryon rescattering is ignored because we are interested in the baryon-baryon invariant mass spectrum. The two-baryon propagator $\mathcal{G}^{\rm OnF}_{B_1B_2}$ applies the on-shell factorization. The integration of $\mathcal{G}^{\rm OnF}_{B_1B_2}$ over the loop momentum q can be regularized simply using the dimensional-regularization method [36] as follows:

$$\begin{aligned} G^{\rm PV,OnF}_{B_1B_2} &\approx i\int\frac{d^4q}{(2\pi)^4}\frac{M_a(M_{4+5}-M_a+M_b)}{[q^2-M_a^2-i\epsilon][(q_{4+5}-q)^2-M_b^2-i\epsilon]} \\ &= \frac{M_a(M_{4+5}-M_a+M_b)}{16\pi^2} \\ &\quad\times\left[\ln\frac{M_b^2}{\mu^2}+\frac{M_a^2-M_b^2+M_{4+5}^2}{2M_{4+5}^2}\ln\frac{M_a^2}{M_b^2}\right. \\ &\quad\left.+\frac{\eta}{M_{4+5}}(L_{+-}+L_{++}-L_{-+}-L_{--})\right] \end{aligned} \tag{25}$$

where we define

$$\begin{aligned} &\eta \equiv \frac{\sqrt{[M_{4+5}^2-(M_a-M_b)^2][M_{4+5}^2-(M_a+M_b)^2]}}{2M_{4+5}}, \\ &L_{\pm\pm} \equiv \ln[\pm M_{45}^2 \pm (M_b^2-M_a^2)+2M_{4+5}\eta]. \end{aligned} \tag{26}$$

Hence, in terms of the on-shell factorization, the coupled-channel amplitude for the $B_1B_2 \to B_3B_4$ channel reads:

$$\begin{aligned} i\hat{\mathcal{M}}^{\rm cc,OnF}_{B_1B_2\to B_3B_4} &= i\hat{\mathcal{M}}_{B_1B_2\to B_3B_4} + \sum_{B_\ell B_{\ell'}}(i\hat{\mathcal{M}}_{B_1B_2\to B_\ell B_{\ell'}}) \\ &\quad\times(G^{\rm OnF}_{B_\ell B_{\ell'}})(i\hat{\mathcal{M}}_{B_\ell B_{\ell'}\to B_3B_4})+\cdots. \end{aligned} \tag{27}$$

Owing to the regularization and Lorentz structure of the elementary amplitudes as shown in Eq. (24), each term in the right-hand side (rhs) of Eq. (27) is finite. Equation (27) can therefore be rewritten in a matrix form as follows:

$$i\hat{\mathbf{M}}^{\rm cc,OnF} = [\mathrm{I}_{3\times3} - (i\hat{\mathbf{M}})(\mathrm{G}^{\rm OnF})]^{-1}(i\hat{\mathbf{M}}). \tag{28}$$

Here, channels (1,2,3) are defined by the $(\Lambda\Lambda, N\Xi, \Sigma\Sigma)$ scattering states.

Regarding the $\Lambda\Lambda \to \Lambda\Lambda$ scattering for FSI, we consider only $i\mathrm{M}_{11}^{\mathrm{cc}} = i\mathcal{M}_{\Lambda\Lambda\to\Lambda\Lambda}^{\mathrm{cc}}$ in Fig. 3. Following extensive calculations, the analytical form is obtained as follows:

$$i\hat{\mathcal{M}}_{\Lambda\Lambda\to\Lambda\Lambda}^{\mathrm{cc,OnF}} = -\frac{\lambda_1[16 - 6i\lambda_1(4G_2 + 3G_3) - 15\lambda_1^2 G_2 G_3]}{128i + 16\lambda_1(G_1 + 4G_2 + 3G_3) + 6i\lambda_1^2(4G_1G_2 + 3G_1G_3 + 12G_2G_3) - 15\lambda_1^3 G_1G_2G_3}, \tag{29}$$

where $G_{1,2,3}$ indicates $G_{\Lambda\Lambda,N\Xi,\Sigma\Sigma}$. Finally, considering all the factors previously indicated, we obtain the FSI-corrected total amplitude for the $\Lambda\Lambda$ channel:

$$i\mathcal{M}_{\mathrm{tree+FSI}}^{\Lambda\Lambda,\mathrm{OnF}} = i\mathcal{M}_{\mathrm{tree}}^{\Lambda\Lambda}\left[1 + \left(G_{\Lambda\Lambda}^{\mathrm{PV,OnF}}\right)\left(i\hat{\mathcal{M}}_{\Lambda\Lambda\to\Lambda\Lambda}^{\mathrm{cc,OnF}}\right)\right]. \tag{30}$$

Similarly, we can derive the $\Xi^- p$ channel total amplitude as follows:

$$i\mathcal{M}_{\mathrm{tree+FSI}}^{\Xi^- p,\mathrm{OnF}} = i\mathcal{M}_{\mathrm{tree}}^{\Xi^- p}\left[1 + \frac{1}{\sqrt{2}}(G_{\Xi^- p}^{\mathrm{PV,OnF}})(i\hat{\mathcal{M}}_{\Xi^- p\to\Xi^- p}^{\mathrm{cc,OnF}})\right], \tag{31}$$

where

$$i\hat{\mathcal{M}}_{\Xi^- p\to\Xi^- p}^{\mathrm{cc,OnF}} = -\frac{\lambda_1[64 + 24i\lambda_1(4G_2 + 3G_3) - 15\lambda_1^2 G_2 G_3]}{128i + 16\lambda_1(G_1 + 4G_2 + 3G_3) + 6i\lambda_1^2(4G_1G_2 + 3G_1G_3 + 12G_2G_3) - 15\lambda_1^3 G_1G_2G_3}. \tag{32}$$

III. NUMERICAL RESULTS AND DISCUSSIONS

In this section, we provide the numerical calculation results with details regarding the $\Lambda p \to K^+\Lambda\Lambda$ ($\Lambda\Lambda$ channel) and $\Lambda p \to K^+\Xi^- p$ ($\Xi^- p$ channel) reaction processes. In this calculation, the H-dibaryon is assumed to be unbound above the $\Lambda\Lambda$ threshold. The mass range of the H-dibaryon is strongly connected with the observation of the double Λ hypernuclei, which imposes that the H-dibaryon mass should be larger than 2.22 GeV/c^2. Recent lattice QCD calculation results indicate that the mass ranges between $\Lambda\Lambda$ and $\Xi^- p$ thresholds [22,30,31,38,39]. Two H-dibaryon states, below and above the $\Xi^- p$ threshold, were chosen considering the $H(2250) \to \Lambda\Lambda$ and $H(2270) \to \Xi^- p$ decays. It is also possible that the interactions between two baryons are too weak to form either a resonance or a bound state. If this is the case, we do not have the pole diagrams (a) and (b) in Fig. 1, and the Λp cross section will be dominated by the baryon-baryon interactions, mediated by the meson exchanges. One can extract the information for the meson-mediated baryon-baryon interactions by analyzing the background contributions even for that the dibaryon does not exist.

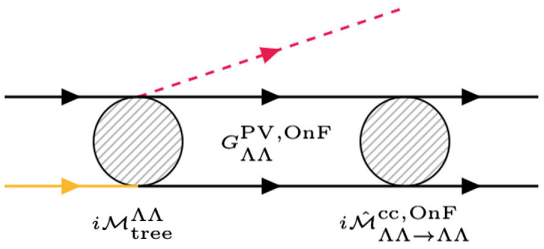

FIG. 3. Schematic for the final-state interaction contribution in Eq. (29), for the $\Lambda\Lambda$ channel.

As indicated in Sec. II, we employ the coupling constants for the dibaryon $g_{BB'H}$ from the bare H-dibaryon model, in which the values were determined to fit the flavor SU(3) symmetric HAL-QCD data [30]. Therefore, the values of $g_{BB'H}$ may be different from reality, where the flavor symmetry is heavily broken. Although the effects of the SU(3) symmetry breaking convert a bound state into a weak resonance dynamically as in Ref. [30], it is rather difficult to describe this effect in the present theoretical framework, since the dibaryon is given as a pole diagram, not generated dynamically. Instead, we explore the two different masses for the dibaryon explicitly as discussed above.

Nonetheless, as guidance for the present theoretical calculations, these symmetric values were adopted as a trial. In Ref. [31], the full decay width of the dibaryon was $\Gamma_H = 2.7$ MeV at the physical point.

First, the cutoff mass was fixed in the form factors in Eq. (7). In Ref. [40], a few events of the $^{12}\mathrm{C}(\Xi^-, \Lambda\Lambda)X$ reaction were reported. Using the eikonal approximation, the total cross section was deduced to $\sigma = 4.3^{+6.3}_{-2.7}$ mb for the $\Xi^- p \to \Lambda\Lambda$ reaction at $p_{\Xi^-} = 0.5$ GeV/c. We reproduced this value in the present theoretical framework. For simplicity, we only considered the κ, K, and K^* exchanges in the t-channel, and ignored a possible H-dibaryon contribution in the s-channel. Moreover, the cutoff masses for the three meson exchanges were chosen to be the same for brevity. The relevant invariant amplitude is then obtained as follows:

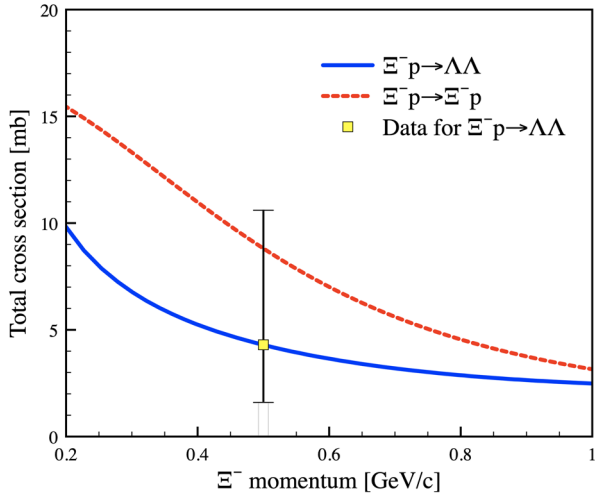

FIG. 4. Total cross section for $\Xi^- p \to \Lambda\Lambda$ (solid) and $\Xi^- p \to \Xi^- p$ (dotted) using Eqs. (33) and (34) with the cutoff mass $\Lambda_{\Lambda\Lambda} = 435$ MeV and $\Lambda_{\Xi^- p} = 535$ MeV, respectively. $\Lambda_{\Lambda\Lambda}$ is determined to reproduce the data point $\sigma = 4.3^{+6.3}_{-2.7}$ mb, extracted from $^{12}\mathrm{C}(\Xi^-, \Lambda\Lambda)X$ data [40].

$$i\mathcal{M}_{\Xi^- p \to \Lambda\Lambda} = \sum_{\Phi=\kappa,K,K^*} i\mathcal{M}_\Phi - (c \leftrightarrow d), \tag{33}$$

where

$$i\mathcal{M}_\Phi = \frac{ig_{\Phi\Xi\Lambda} g_{\Phi N\Lambda} (\bar{u}_c \Gamma_\Phi u_a)(\bar{u}_d \Gamma^\Phi u_b) F_\Phi(t)}{t - M_\Phi^2 - i\Gamma_\Phi M_\Psi},$$
$$\Gamma_{\kappa,K,K^*} = (\mathbf{1}_{4\times4}, \gamma_5, \gamma_\mu). \tag{34}$$

All relevant inputs are listed in Tables I and II. Thus, the cutoff mass for the $\Lambda\Lambda$ channel, i.e., $\Lambda_{\Lambda\Lambda}$ is determined to be 435 MeV to reproduce the $\Xi^- p \to \Lambda\Lambda$ cross section $\sigma = 4.3^{+6.3}_{-2.7}$ mb as shown by the solid line in Fig. 4. As for the $\Xi^- p$ channel, we employed the analyses of Ref. [40], indicating that the upper limit of the elastic scattering cross section is about two-times larger than that for $\Xi^- p \to \Lambda\Lambda$. Hence, we determine the cutoff value $\Lambda_{\Xi^- p}$ to reproduce the cross section $\sigma \approx 9$ mb at $p_{\Xi^-} = 0.5$ GeV/c resulting in $\Lambda_{\Xi^- p} = 535$ MeV as shown by the dashed lines in the figure.

In the left panel of Fig. 5, the numerical results for the total cross sections of the $\Lambda\Lambda$ (square) and $\Xi^- p$ (circle) channels are presented for the total (thick) and H-dibaryon-only (thin) contributions as a function of the Λ beam momentum p_{lab}. We determined that the total cross sections for the two channels are of the order of approximately a few μb, which is smaller than that for the $pp \to K^+\Lambda p$ from the COSY experiment [41]. The total cross sections from the $\Lambda\Lambda$ channel are approximately twice as large as that of the $\Xi^- p$ because there are more possible contributions, as shown in the relevant Feynman diagrams in Fig. 1, in addition to the larger Nijmegen coupling constants. On the

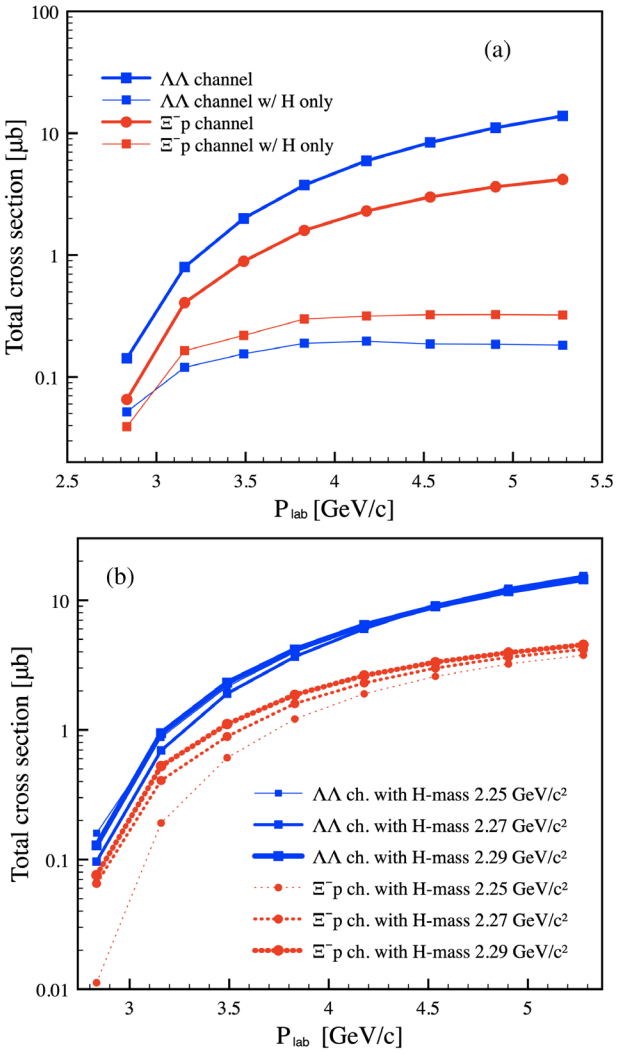

FIG. 5. (a) Total cross sections for the $\Lambda\Lambda$ (square) and $\Xi^- p$ (circle) channels for the total (thick) and H-dibaryon-only (thin) contributions as functions of the Λ beam momentum p_{lab}. (b) Total cross sections by varying the masses of the H dibaryon.

contrary, if we only consider the H-dibaryon, the order of the cross sections is reversed, owing to the value of $g_{H\Lambda\Lambda}$ being smaller than $g_{H\Xi^- p}$ by a factor of two considering the isospin factor. Note, the production cross section for the H dibaryon is *a few tens of nanobarn*. As shown in the right panel of Fig 5, to test the H-dibaryon mass dependence of the total cross sections, they are depicted with $M_H = (2.25 \sim 2.29)$ GeV/c^2 for the two reaction channels. The effects from the mass changes are unapparent, while considerable difference can be observed for the $\Xi^- p$ channel with $M_H = 2.25$ GeV/c^2.

In Fig. 6, the numerical results for the differential cross sections of the $\Lambda\Lambda$ (left) and $\Xi^- p$ (right) channels are presented as the function of the scattering angle of K^+ in the center-of-mass frame (cm) θ. We also analyzed the differential cross sections in the energy range of $E_{\mathrm{cm}} = 2.8$–3.0 GeV. The thick and thin lines denote the

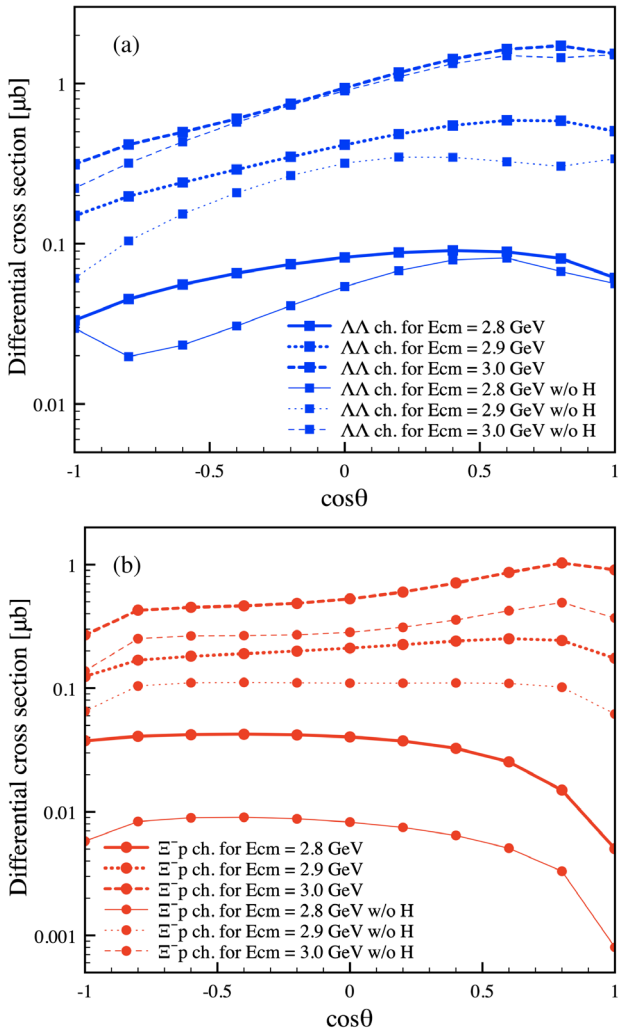

FIG. 6. Differential cross sections for (a) $\Lambda\Lambda$ and (b) $\Xi^- p$ (right) channels, respectively, as functions of the scattering angle of K^+ in the center-of-mass frame (cm) θ.

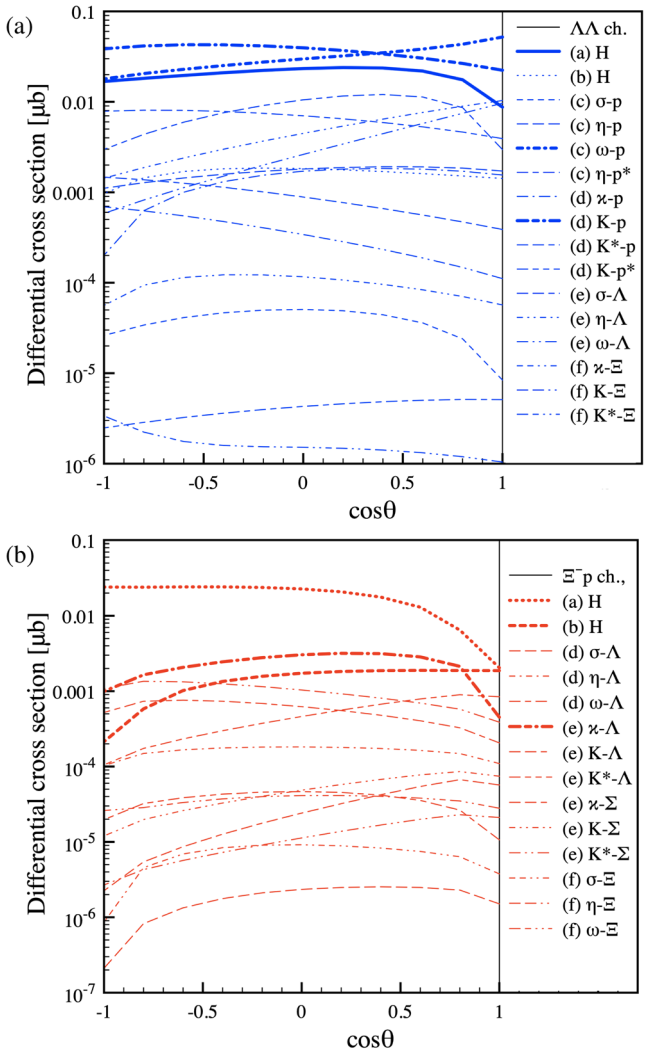

FIG. 7. Differential cross sections for (a) the $\Lambda p \to K^+\Lambda\Lambda$ and (b) $\Lambda p \to K^+\Xi^- p$ reactions at $E_{\rm cm} = 2.8$ GeV ($p_\Lambda = 2.83$ GeV/c) are plotted in separate curves for individual diagram contributions.

cases with and without the H-dibaryon contributions, respectively. The angular dependence for the two channels is relatively flat at a low energy and forwarding as the energy increases. Note, the angular dependence of the H-dibaryon production is nearly flat at high energies, indicating the S-wave nature of the particle.

To investigate the production mechanisms more carefully, we present the numerical results for the differential cross sections for each contribution individually at $E_{\rm cm} = 2.8$ GeV ($p_{\rm lab} = 2.83$ GeV/c), in the same manner as presented in Fig 7. Regarding the $\Lambda\Lambda$ channel, the ω and K^- exchanges in the proton-pole diagrams (c and d) are predominant owing to the combinations of the larger Nijmegen coupling constants. Moreover, the H-dibaryon production diagram with the Λ pole (a) is significantly larger than that of the Ξ^--pole diagram (b). Regarding the $\Xi^- p$ channel, the H-dibaryon production diagrams are considerably larger than others, and the κ exchange in the t channel (e) provides a meaningful contribution. Generally, we determined that the H-dibaryon production diagram (a) with the Mandelstam variable $t = (k_\Lambda - k_{K^+})^2$ enhances forward scattering, and vice versa for the diagram (b) with $u = (k_p - k_{K^+})^2$, as expected.

The Dalitz plot for the $\Lambda p \to K^+\Lambda\Lambda$ and $\Lambda p \to K^+\Xi^- p$ reactions are plotted in Fig. 8 for a Λ beam momentum of 2.83 GeV/c. Because no background processes form structure in the Dalitz plots, the H-dibaryon band appears predominant. The numerical results for the invariant-mass plots are provided in Fig. 9 with $M_H = 2.25$ GeV/c^2 and 2.27 GeV/c^2 for the $\Lambda\Lambda$ (left) and $\Xi^- p$ (right) channels, respectively, at $E_{\rm cm} = 2.8$ GeV. The width of the H dibaryon is assumed to be 1 MeV, whereas the phase angle ϕ is tested for 0 (thick) and π (thin). The shaded areas indicate the cases without the H dibaryon. The light and heavy shared areas indicate the cases without and only with the H dibaryon. We observed that the H-dibaryon

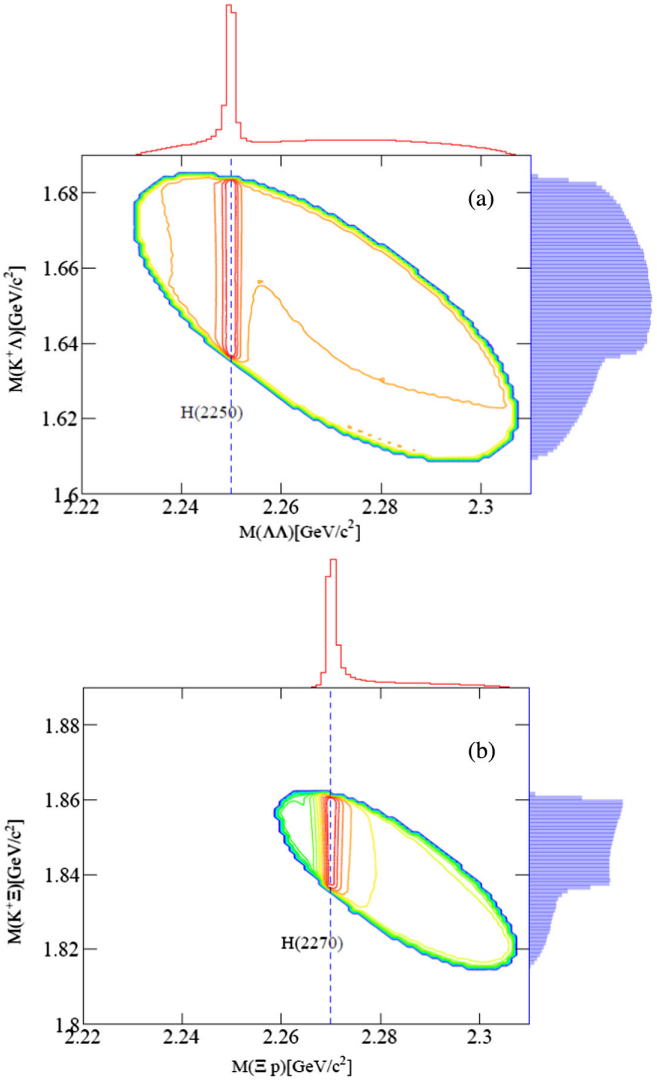

FIG. 8. Dalitz plots for (a) the $\Lambda p \to K^+\Lambda\Lambda$ and (b) $\Lambda p \to K^+\Xi^- p$ reactions at $p_\Lambda = 2.83$ GeV/c, respectively. Both contain the relative phase angle $\psi = 0$. The Dalitz plots are projected onto the $\Lambda\Lambda/\Xi^- p$ and $K^+\Lambda/K^+\Xi^-$ mass axes and plotted as histograms on the top and right sides, respectively.

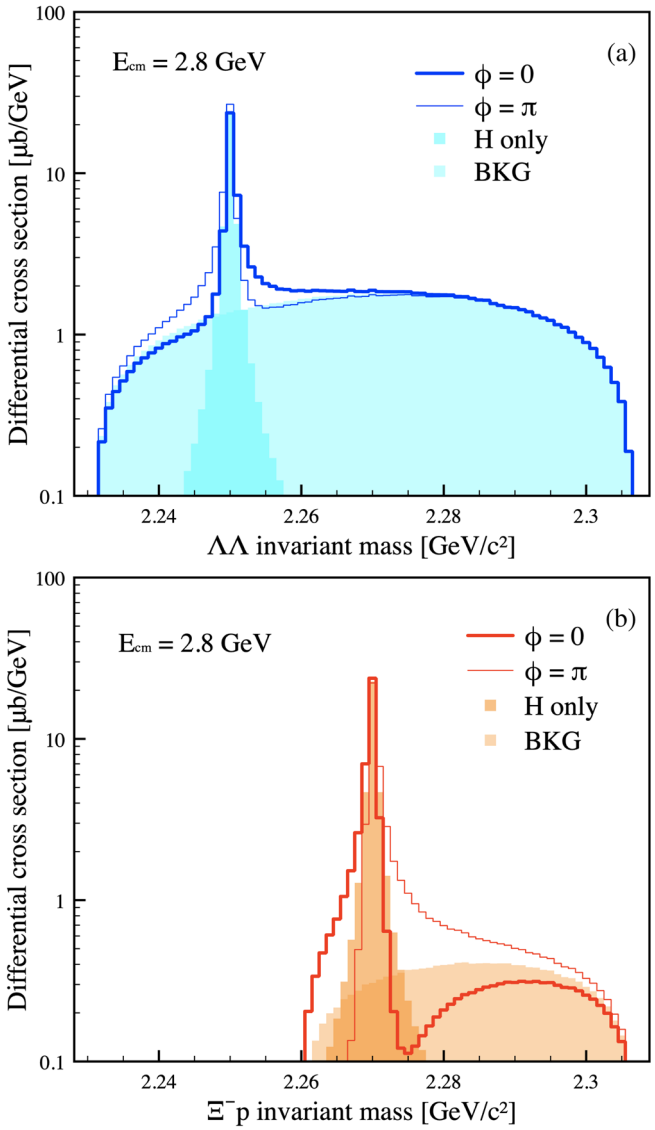

FIG. 9. Invariant-mass plots for $M_H = 2.25$ GeV/c^2 and 2.27 GeV/c^2 for (a) $\Lambda\Lambda$ and (b) $\Xi^- p$ channels, respectively, at $E_{\rm cm} = 2.8$ GeV. The width of the H dibaryon is chosen to be 1 MeV and the phase angle ϕ is tested for 0 (thick) and π (thin). The shaded areas indicate the cases without the H-dibaryon.

production rates are larger for the $\Xi^- p$ channel by a factor of two, than that for the $\Lambda\Lambda$ channel, and vice versa for the total background contributions, as shown in Fig. 9. The signal-to-background ratio is approximately 0.3 for the $\Lambda\Lambda$ channel, whereas the larger value of 1.6 is for the $\Xi^- p$ channel. Therefore, the $\Xi^- p$ channel enables us to search for the H dibaryon significantly easier than the $\Lambda\Lambda$ channel. The production cross sections for $H(2250) \to \Lambda\Lambda$ and $H(2270) \to \Xi^- p$ are approximately 40 nb and 38 nb, respectively. Significant changes are obtained by the different phase factors, clearly shown in the $\Xi^- p$ channel, owing to the smaller interference with the background processes. Furthermore, we note that the channel opening effects from the final-state interactions were small, resulting in cusplike structures being hardly observed.

Finally, considering the decay-angle distribution of the H-dibaryon, the decay angle distribution of the S-wave H-dibaryon is isotropic at the rest frame of the H-dibaryon. We define the double differential cross section as $d^2\sigma/d\cos\theta_{\rm cm} d\cos\psi_{\rm rest}$, where the angle $\theta_{\rm cm}$ denotes that of the outgoing K^+ in the cm frame. The angle $\psi_{\rm rest}$ is defined by

$$\psi_{\rm rest} \equiv \frac{\vec{k}^{B_f}_{\rm rest} \cdot \vec{k}^{K^+}_{\rm cm}}{|\vec{k}^{B_f}_{\rm rest}||\vec{k}^{K^+}_{\rm cm}|}, \tag{35}$$

where $\vec{k}^{B_f}_{\rm rest}$ and $\vec{k}^{K^+}_{\rm cm}$ indicate the three momenta of the one decaying baryon in the final state at the H-dibaryon rest frame and the outgoing K^+ in the cm frame, respectively.

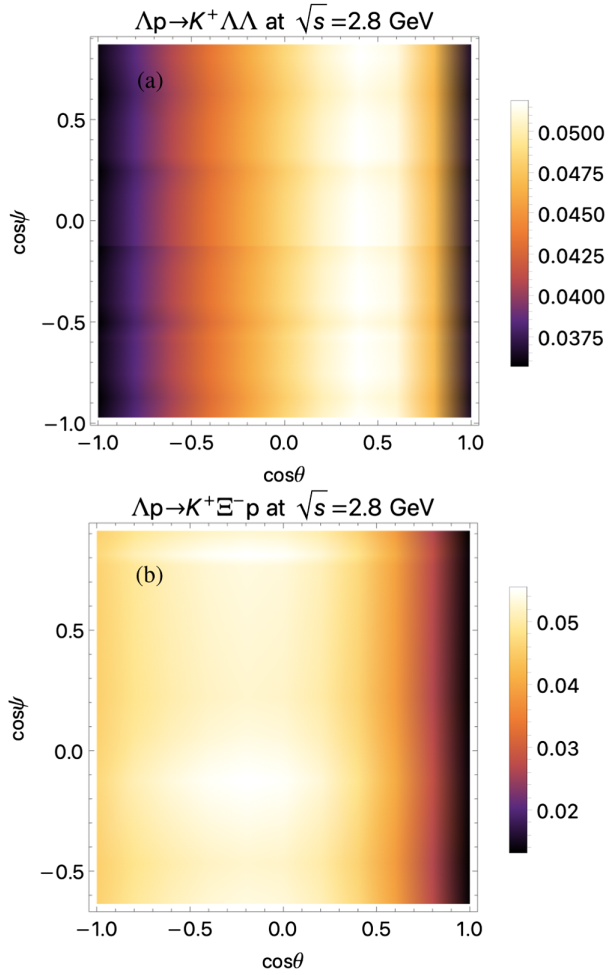

FIG. 10. Double differential cross section [μb] as a function of $\cos\theta_{\rm cm}$ and $\cos\psi_{\rm rest}$ for (a) the $\Lambda\Lambda$ and (b) $\Xi^- p$ channels. See the text for details.

In Fig. 10, we depict the numerical results for the double differential cross sections as a function of $\cos\theta_{\rm cm}$ and $\cos\psi_{\rm rest}$ with the H-dibaryon contribution only. As expected, we clearly observe that the decay-angle distribution, i.e., the double differential cross sections, are nearly flat for the various $\cos\theta_{\rm cm}$ values.

IV. SUMMARY

In this study, we investigated the $H(I=0, J=0)$-dibaryon production via $\Lambda p \to \Lambda\Lambda K^+$ theoretically. Thus, we employed the effective Lagrangian approach at the tree-level Born approximation. We considered the mass and decay width of the dibaryon as the theoretical input parameters, and they were chosen by considering presently available theoretical and experimental results, such as the lattice-QCD data analyses with the flavor SU(3) breaking effects: $2M_\Lambda \le M_H \le (M_{\Xi^-} + M_p)$ and $\Gamma_H = (1\text{–}10)$ MeV. The critical observations made in this study are as follows:

(i) The total cross sections for the $\Lambda\Lambda$ and $\Xi^- p$ channels are determined to be within the order of a few μb in the Λ beam momentum of up to 5 GeV/c, while the production cross section for the H-dibaryon is approximately 100 nb. Here, we determined our model parameters such as the cutoff masses for the form factors, based on the experimental data for the $\Xi^- p$ elastic and $\Xi^- p \to \Lambda\Lambda$ scattering cross sections.

(ii) The total cross sections do not change significantly with the H-dibaryon mass from 2.25 GeV/c^2 to 2.27 GeV/c^2. Because the $\Lambda\Lambda$ production channel involves more background processes than the $\Xi^- p$ channel, by ignoring the channel via an exotic pentaquark-state, the H-dibaryon contribution appears to be relatively large in the $\Xi^- p$ channel.

(iii) We observed that the differential cross sections for the $\Lambda p \to K^+\Lambda\Lambda$ and $\Lambda p \to K^+\Xi^- p$ channels peak at the forward K^+ angles in the cm frame, owing to the t-channel meson and baryon exchange processes. The H-dibaryon-pole contributions are significant near the threshold and depend minimally on the K^+ angle.

(iv) From the invariant mass distributions, the signal-to-background ratios are approximately 0.3 and 1.6 for the $\Lambda\Lambda$ and $\Xi^- p$ channels, respectively, owing to the smaller background contributions in the $\Xi^- p$ channel. Note, the H-dibaryon peak areas yield 40 nb and 38 nb for the $\Lambda\Lambda$ and $\Xi^- p$ channels, respectively.

(v) We also explored the change in the interference patterns between the H-dibaryon and background amplitudes with the relative phase angle for the $\Xi^- p$ channel. The channel opening effects from the final-state interactions were small; therefore, cusplike structures were hardly observed.

(vi) Lastly, we calculated the decay angular distributions of the $H \to \Lambda\Lambda$ and $H \to \Xi^- p$ decays in the helicity frame in which the quantization axis is in the opposite direction of K^+ in the H-dibaryon rest frame. The angular distributions are flat over the H-dibaryon mass region, as expected for the S-wave resonance.

Considering the aforementioned factors, we conclude that the H-dibaryon could be clearly identified in the $\Lambda p \to K^+\Lambda\Lambda$ and $\Lambda p \to K^+\Xi^- p$ reactions close to the production threshold, if it exists close to the $\Xi^- p$ threshold. Further studies related to other H-dibaryon production reactions are in progress and will appear elsewhere.

ACKNOWLEDGMENTS

S.-i. N. is grateful for useful discussions with T. Hyodo. This work was supported in part by the National Research Foundation of Korea (NRF) grants funded by the Korean government (No. 2018R1A5A1025563, No. 2019R1A2C1005697, No. 2020R1A3B2079993).

[1] D. E. Kahana and S. H. Kahana, AIP Conf. Proc. **644**, 270 (2002).
[2] S. Acharya *et al.* (ALICE Collaboration), Phys. Rev. Lett. **123**, 112002 (2019).
[3] S. H. Hayakawa *et al.* (E07 Collaboration), Phys. Rev. Lett. **126**, 062501 (2021).
[4] K. Nakazawa *et al.*, Prog. Theor. Exp. Phys. **2015**, 33D02 (2015).
[5] H. Takahashi *et al.*, Phys. Rev. Lett. **87**, 212502 (2001).
[6] H. Ekawa *et al.*, Prog. Theor. Exp. Phys. **2019**, 021D02 (2019).
[7] S. Aoki *et al.* (KEK E176 Collaboration), Nucl. Phys. **A828**, 191 (2009); Prog. Theor. Phys. **85**, 1287 (1991).
[8] K. W. Li, T. Hyodo, and L. S. Geng, Phys. Rev. C **98**, 065203 (2018).
[9] J. Haidenbauer, U. G. Meißner, and S. Petschauer, Nucl. Phys. **A954**, 273 (2016).
[10] V. Baru, E. Epelbaum, J. Gegelia, and X. L. Ren, Phys. Lett. B **798**, 134987 (2019).
[11] M. Oka and S. Takeuchi, Nucl. Phys. **A524**, 649 (1991).
[12] L. Adamczyk *et al.* (STAR Collaboration), Phys. Rev. Lett. **114**, 022301 (2015).
[13] S. Acharya *et al.* (ALICE Collaboration), Phys. Lett. B **797**, 134822 (2019).
[14] H. Suganuma and K. Matsumoto, EPJ Web Conf. **137**, 13018 (2017).
[15] K. Matsumoto, Y. Nakagawa, and H. Suganuma, J. Phys. Soc. Jpn. Conf. Proc. **13**, 020014 (2017).
[16] W. Park, A. Park, and S. H. Lee, Phys. Rev. D **93**, 074007 (2016).
[17] P. B. Mackenzie and H. B. Thacker, Phys. Rev. Lett. **55**, 2539 (1985).
[18] Y. Iwasaki, T. Yoshie, and Y. Tsuboi, Phys. Rev. Lett. **60**, 1371 (1988).
[19] Z.-H. Luo, M. Loan, and Y. Liu, Phys. Rev. D **84**, 034502 (2011).
[20] T. Inoue, N. Ishii, S. Aoki, T. Doi, T. Hatsuda, Y. Ikeda, K. Murano, H. Nemura, and K. Sasaki (HAL QCD Collaboration), Prog. Theor. Phys. **124**, 591 (2010).
[21] A. Francis, J. R. Green, P. M. Junnarkar, C. Miao, T. D. Rae, and H. Wittig, Phys. Rev. D **99**, 074505 (2019).
[22] K. Sasaki *et al.* (HAL QCD Collaboration), Nucl. Phys. **A998**, 121737 (2020).
[23] J. K. Ahn *et al.* (E224 Collaboration), Phys. Lett. B **444**, 267 (1998).
[24] C. J. Yoon *et al.* (E522 Collaboration), Phys. Rev. C **75**, 022201 (2007).
[25] J. K. Ahn and K. Imai, J-PARC Proposal E42, Search for the H-dibaryon with a Large Acceptance Hyperon Spectrometer; J. K. Ahn, Few-Body Syst. **54**, 387 (2013); J. Phys. Soc. Jpn. Conf. Proc. **17**, 031004 (2017).
[26] K. Miyano *et al.*, Phys. Rev. C **38**, 2788 (1988).
[27] R. Honda *et al.*, Letter of Intent for a Λp scattering experiment at J-PARC submitted in 2020.
[28] J. Price (for CLAS Collaboration), AIP Conf. Proc. **2130**, 020004 (2019).
[29] S. Y. Ryu (for LEPS2 Collaboration), AIP Conf. Proc. **2249**, 030024 (2020).
[30] Y. Yamaguchi and T. Hyodo, Phys. Rev. C **94**, 065207 (2016).
[31] T. Inoue, S. Aoki, T. Doi, T. Hatsuda, Y. Ikeda, N. Ishii, K. Murano, H. Nemura, and K. Sasaki (HAL QCD Collaboration), Nucl. Phys. **A881**, 28 (2012).
[32] V. G. J. Stoks and T. A. Rijken, Phys. Rev. C **59**, 3009 (1999).
[33] P. A. Zyla *et al.* (Particle Data Group), Prog. Theor. Exp. Phys. **2020**, 083C01 (2020).
[34] E. J. Garzon and E. Oset, Phys. Rev. C **91**, 025201 (2015).
[35] C. An and B. Saghai, Phys. Rev. C **84**, 045204 (2011).
[36] S. I. Nam, H. C. Kim, T. Hyodo, D. Jido, and A. Hosaka, J. Korean Phys. Soc. **45**, 1466 (2004).
[37] K. Sasaki, S. Aoki, T. Doi, T. Hatsuda, Y. Ikeda, T. Inoue, N. Ishii, and K. Murano (HAL QCD Collaboration), Prog. Theor. Exp. Phys. **2015**, 113B01 (2015).
[38] P. E. Shanahan, A. W. Thomas, and R. D. Young, Phys. Rev. Lett. **107**, 092004 (2011).
[39] J. Haidenbauer and U. G. Meissner, Phys. Lett. B **706**, 100 (2011).
[40] J. K. Ahn *et al.*, Phys. Lett. B **633**, 214 (2006).
[41] J. T. Balewski *et al.* Phys. Lett. B **388**, 859 (1996).